Supplementary Materials for

Atomic Interface Effect of Single Atom Copper Catalyst for Enhanced Oxygen Reduction Reaction

Zhuoli Jiang, ‡ [a] Wenming Sun, ‡ [c] Huishan Shang, ‡ [a] Wenxing Chen, *[a] Tingting Sun, [d] Haijing Li, [e] Juncai Dong, [e] Jing Zhou, [f] Zhi Li, [b] Yu Wang, [f] Rui Cao, [g] Ritimukta Sarangi, [g] Zhengkun Yang, [h] Dingsheng Wang, *[b] Jiatao Zhang, *[a] and Yadong Li *[b]

[a] Beijing Key Laboratory of Construction Tailorable Advanced Functional Materials and Green Applications, School of Materials Science and Engineering, Beijing Institute of Technology, Beijing 100081, China

[b] Department of Chemistry, Tsinghua University, Beijing 100084, China

[c] College of Science, China Agricultural University, Beijing 100193, China

[d] Beijing Key Laboratory for Science and Application of Functional Molecular and Crystalline Materials, Department of Chemistry, University of Science and Technology Beijing, Beijing 100083, China

[e] Beijing Synchrotron Radiation Facility, Institute of High Energy Physics, Chinese Academy of Sciences, Beijing 100049, China

[f] Shanghai Synchrotron Radiation Facilities, Shanghai Institute of Applied Physics, Chinese Academy of Science, Shanghai 201800, China

[g] Stanford Synchrotron Radiation Lightsource, SLAC National Accelerator Laboratory, Menlo Park, CA, 94025, USA

[h] Department of Chemistry, Collaborative Innovation Center of Chemistry for Energy Materials, University of Science and Technology of China, Hefei 230026, China

‡ These authors contributed equally to this work.

* Corresponding author. E-mail: wxchen@bit.edu.cn, zhangjt@bit.edu.cn, wangdingsheng@mail.tsinghua.edu.cn, ydli@mail.tsinghua.edu.cn.

Table of contents

Section1. Experiment detail

Materials

Copper phthalocyanine (CuPc), dicyandiamide (DCDA), sulfur powder, sodium sulfide ($Na_2S \cdot 9H_2O$), afion D-521 dispersion (5% w/w in water and 1-propanol) and commercial Pt/C (20 wt% metal) were purchased from Alfa Aesar. Methanol, ethanol and KOH were obtained from Sinopharm Chemical. Sulphuric acid (H_2SO_4) (98%) was obtained from Beijing Chemical Reagents. The deionized water used in all experiments was obtained through ion-exchange and filtration. All the chemicals were analytical grade and used without further purification.

Preparation of S precursor

In a typical synthesis, $Na_2S \cdot 9H_2O$ (140.4mg) was dissolved in deionized (DI) water (11.7 ml) and subsequently S powder (32mg) was added in the above solution while ultrasonic dissolving. After ultrasonic dissolving for 5h at ambient conditions, the yellow clear and transparent solution was heated at 80 °C for 12 h in a Teflon autoclave. The S precursor was obtained after the solution was cooled down to room temperature.

Preparation of Cu-SA/SNC

In a typical procedure, 50 mg CuPc, 1.2 g DCDA and 0.12g trimesic acid were dissolved in 5 mL of deionized water. 2ml S precursor was added then mixed together under vigorous stirring. The solution was continuously stirred and dried at 80 °C. The obtained dried mixture was placed in the porcelain boat. The porcelain boat was placed in a quartz tube of a horizontal furnace. And then, the boat was annealed at 900 °C under the N_2 atmosphere for 2 h with a ramping rate of 5 °C/min, then cooled down to room temperature. Subsequently, the samples were leached in 0.5 M H_2SO4 solution at 80 °C for 24 h to remove the free standing metallic residues, and washed thoroughly with ethanol and deionized water. Finally, the samples were dried in vacuum at 60 ºC for overnight.

Preparation of Cu-SA/NC

Typically, 50 mg CuPc, 1.2 g DCDA and 0.12 g trimesic acid were dissolved in 5 mL of deionized water. The mixed solution was continuously stirred and dried at 80 °C. The mixture was transferred into a porcelain boat and placed in a tube furnace. Then the powder was heated from room temperature to 900 °C with a heating rate of 5 °C /min under the N_2 atmosphere. After calcining for further 2 h at the desired temperature, the sample was naturally cooled to room temperature. Subsequently, the samples were leached in 0.5 M H_2SO4 solution at 80 °C for 24 h. Finally, the samples were washed and dried.

Preparation of NC

Trimesic acid (0.12 g) and DCDA (1.2 g) were mixed by grinding and annealed from room temperature to 900 °C with a heating rate of 5 °C /min under a N_2 flow. After calcining for further 2 h at the desired temperature, the sample was naturally cooled to room temperature, denoted as NC.

Preparation of SNC

Trimesic acid (0.12 g) and DCDA (1.2 g) were dissolved in 5 mL of deionized water. 2 ml S precursor was added then mixed together under vigorous stirring. The mixture was annealed at 900 °C under the N_2 atmosphere for 2 h with a ramping rate of 5 °C/min, then cooled down to room temperature, denoted as SNC.

Characterization

The morphology of the samples was characterized by transmission electron microscope (TEM, FEI Tecnai G2 20) with an accelerating voltage of 200 kV. The HAADF-STEM images were obtained by JEOL JEM-ARM200F at an accelerating voltage of 200 kV. The crystal phases present in each sample were identified using powder X-ray diffraction (XRD) patterns were recorded on a Y-2000 X-ray Diffractometer with copper Kα radiation (λ=1.5406 Å) at 40 kV, 40 mA. The Raman measurements were taken on a Renishaw spectrometer at 532 nm on a Renishaw Microscope System RM2000. The N_2 adsorption/desorption curve was carried out by BET measurements using a Micromeritics ASAP 2020 surface area analyzer.

Electrochemical measurements for ORR

2 mg of the catalyst and 10 μl Nafion solution (5 wt %) ultrasonically dispersed in the mixture of deionized water/ethanol(volume ratio, 1 : 4) for at least 30 min to yield a

well-dispersed catalyst ink with a concentration of 2 mg mL^{-1}. Electrochemical measurements were carried out on CHI 760E electrochemical workstation (Shanghai Chenhua, China) with a typical three-electrode electrochemical cell in 0.1 M KOH electrolyte. A graphite rod and an Ag/AgCl (saturated KCl) electrode were used as the counter electrode and reference electrode, respectively. 10 μL of the catalyst ink prepared above was dropped on a glassy carbon (GC) electrode with a surface area of 0.196 cm^2 and the catalyst loading was 0.102 mg cm^{-2}. Before all measurements, N_2/O_2 flow were used through the electrolyte in the cell for 30 min to obtain N_2/O_2-saturated electrolyte. The cyclic voltammetry (CV) experiments were cycled in N_2/O_2-saturated 0.1 M KOH with a scan rate of 50 $mV\cdot s^{-1}$, and the linear sweep voltammetry (LSV) experiments were cycled in O_2-saturated 0.1 M KOH with a scan rate of 10 $mV\cdot s^{-1}$. The LSV measurements of the catalysts were determined using a rotating disk electrode (RDE) (Pine Research Instrumentation) and the rotating speed was varied from 400 to 2500 rpm. The number of electrons transferred (n) and kinetic current density (J_k) during ORR was calculated according to Koutecky-Levich equation：

$$\frac{1}{J} = \frac{1}{J_L} + \frac{1}{J_K} = \frac{1}{B\omega^{1/2}} + \frac{1}{J_K} \tag{1}$$

$$B = 0.62nFC_0D_0^{2/3}V^{-1/6} \tag{2}$$

where J is the measured current density, J_K and J_L are the kinetic and diffusion-limiting current densities, ω is the angular velocity (ω=2πN, N is the rotation speed), n is transferred electron number, F is the Faraday constant (96485 C mol^{-1}), C_0 is the bulk concentration of O_2 ((1.2×10^{-6} mol cm^{-3}), D_0 is the diffusion coefficient of O_2 in 0.1 M KOH (1.9×10^{-5} cm^2 s^{-1}), and ν is the kinematic viscosity of the electrolyte (0.01 cm^2 s^{-1}).

For further determine the four-electron selectivity, rotating ring-disk electrode (RRDE) measurements were performed in the O_2-saturated 0.1 M KOH. The disk electrode was scanned at a rate of 10 mV s^{-1}, and the ring electrode potential was set to 1.2 V vs. RHE. The Hydrogen peroxide yield ($\%H_2O_2$) and the electron transfer number (n) were determined by the followed equations:

$$\%\mathrm{H_2O_2} = 200\frac{\mathrm{i_r}/\mathrm{N}}{\mathrm{i_d}+\mathrm{i_r}/\mathrm{N}} \tag{3}$$

$$\mathrm{n} = 4\frac{\mathrm{i_d}}{\mathrm{i_d}+\mathrm{i_r}/\mathrm{N}} \tag{4}$$

Where i_d and i_r are the disk and ring currents, respectively. N is the ring current collection efficiency, which was determined to be 37% by the reduction of 10 mM $K_3[Fe(CN)_6]$ in 0.1 M KNO_3.

Zn-air battery measurements

The primary Zn-air battery measurements were carried out in a home-made electrochemical cell. The Cu-SA/SNC catalyst ink was uniformly dispersed onto teflon-coated carbon fiber paper (1.0 cm), then was dried at 60 °C for 2 h. The catalyst loading was 1.0 mg cm^{-2}. For comparsion, 20% Pt/C electrode with same catalyst loading was also prepared. Polished commercial Zn foil with thickness of 0.2 mm was employed as anode. Both electrodes were constructed in 6 M KOH electrolyte saturated with O_2 (Fig S13).

Soft-XAS measurements

The soft XANES spectra (C K-edge, N K-edge and S L-edge) were measured at beamline BL12B of National Synchrotron Radiation Laboratory (NSRL). A bending magnet is connected to the beamline, which is equipped with three gratings covering photon energy range from 100 to 1000 eV with an energy resolution of ~0.2 eV. The resolving power of the grating was typically $E/\Delta E = 1000$, and the photon flux was 1×10^{-10} photons per second. The Cu L-edge XANES spectra of Cu-SA/SNC were collected at the BL11A beamline of National Synchrotron Radiation Research Center (NSRRC). All the samples for solf XAS test were deposited onto double-sided carbon tape and the data were recorded in the total electron yield mode.

XAFS measurements

The XAFS spectra data (Cu K-edge) were collected at BL14W1 station in Beijing Synchrotron Radiation Facility (SSRF, operated at 3.5 GeV with a maximum current of 250 mA) and BL7-3 station in Stanford Synchrotron Radiation Lightsource (SSRL, operated at 3 GeV with a current of ~500 mA), respectively. The XAFS data of the samples were collected at room temperature in fluorescence excitation mode using a

Lytle detector.

The in-situ cell possesses transparent flat walls with a single circular hole (1.5 cm in diameter). The Cu-SA/SNC coated carbon paper with the catalyst layer facing inward was contacted with a copper conductor. 0.1 M KOH solution was poured into the cell (O_2-saturated), without stirring during all the experiments. A cap fitted with reference and counter electrodes was employed to cover the cell and ensure a fixed distance between the three electrodes during the measurements. Before the in-situ XAS measurements, the spectra were recorded at different positions on the working electrode to check the homogeneity of the catalyst. At each potential, three scans were collected at the Cu K-edge. After each potential change, the system was allowed to equilibrate for 20 min before the recording of a next spectrum.

XAFS data processing

The acquired EXAFS data were processed according to the standard procedures using the Athena and Artemis implemented in the IFEFFIT software packages. The fitting detail is described below:

The acquired EXAFS data were processed according to the standard procedures using the ATHENA module implemented in the IFEFFIT software packages. The EXAFS spectra were obtained by subtracting the post-edge background from the overall absorption and then normalizing with respect to the edge-jump step. Subsequently, the χ(k) data of were Fourier transformed to real (R) space using a hanning windows (dk=1.0 $Å^{-1}$) to separate the EXAFS contributions from different coordination shells. To obtain the quantitative structural parameters around central atoms, least-squares curve parameter fitting was performed using the ARTEMIS module of IFEFFIT software packages.[1]

The following EXAFS equation was used:

$$\chi(k)=\sum_j \frac{N_j S_o^2 F_j(k)}{k R_j^2}\exp[-2k^2\sigma_j^2]\exp[\frac{-2R_j}{\lambda(k)}]\sin[2kR_j+\phi_j(k)]$$

S_0^2 is the amplitude reduction factor, $F_j(k)$ is the effective curved-wave backscattering amplitude, N_j is the number of neighbors in the j^{th} atomic shell, R_j is the distance between the X-ray absorbing central atom and the atoms in the j^{th} atomic shell (backscatterer), λ is the mean free path in Å, $\phi_j(k)$ is the phase shift (including the phase shift for each shell and the total central atom phase shift), σ_j is the Debye-Waller parameter of the j^{th} atomic shell (variation of distances around the average R_j). The functions $F_j(k)$, λ and $\phi_j(k)$ were calculated with the ab initio code FEFF8.2. The additional details for EXAFS simulations are given below.

The coordination numbers of model samples (Cu foil) were fixed as the nominal values. The obtained S_0^2 was fixed in the subsequent fitting of Cu single atom samples. While the internal atomic distances R, Debye-Waller factor σ^2, and the edge-energy shift ΔE_0 were allowed to run freely.

Wavelet transform (WT) analysis

Wavelet transform (WT) for the k^3-weighted EXAFS signals of Cu-SA/SNC, CuPc and Cu foil are carried on the complex wavelet developed by Morlet, which consists of a slowly varying amolitude term and a fast oscillating phase term similar to an EXAFS signal.[2] Moelet parameters sets are optmized for k-space resolution (η=5, σ=1). WT was done in R space 1.0-3.5 Å and k-weight of 3, with k range of 0-12 Å^{-1}.[3] The wavelet transform analysis were processed using the IGOR pro software.[4-6]

The detail of DFT calculations

Spin-polarized density functional theory (DFT) calculations were performed using CASTEP module.[7] The Vanderbilt-type ultrasoft pseudopotential was employed, and the wave functions were expanded in a plane wave basis with an energy cutoff of 400 eV. The electron exchange-correlation potential was described by GGA-PBE functional.[8] The Cu-SA/SNC model was constructed by embedding a CuN_4 atomic structure in a 6 × 6 supercell of graphene. A vacuum region of 15 Å was created along the surface to avoid interactions between the slabs. The diploe correction was applied for the electrostatic potential as well as the total energy and tis gradients. The Brillouin zone integrations were performed over 1 × 1 × 1 grid points using the Monkhorst-Pack scheme for Cu-SA/SNC based systems. The coordinates of all atoms were relaxed during the optimization. Structure relaxations were performed until the maximum force on each atom was less than 0.03 eV/Å, respectively. Brillouin zone integration was sampled with 1×1×1. Computational hydrogen electrode (CHE) model were used to study the thermodynamics of ORR on catalysts. In CHE model, free energy of proton and electron pair is equivalent to that of the half of $H_2(g)$ under standard reaction conditions. For ORR in an alkaline electrolyte, the overall reaction scheme is $O_2 + 2H_2O + 4e^- = 4OH^-$. The overall reaction is divided into four elementary steps:

(1) $O_2(g) + H_2O(l) + e^- + * = OOH* + OH^-$

(2) $OOH* + e^- = O* + OH^-$

(3) $O* + H_2O(l) + e^- = OH* + OH^-$

(4) $OH*+ e^- = * + OH^-$

Where * stands for the active site on the catalytic surface, (g) and (l) refer to gas and liquid phase, respectively.

The free energy diagrams of ORR were calculated according to the method developed by Norskov et al (*J Phys Chem B (2004) 108, 17886-17892*) as follows:

$\Delta G = \Delta E + \Delta ZPE - T\Delta S + \Delta G_U + \Delta G_{pH}$

Where ΔE is the total energy change obtained from DFT calculations, ΔZPE and ΔS are the change in zero point energy and entropy, respectively. $\Delta G_U = -neU$, where U is the applied electrode potential, n is the number of electrons transferred. ΔG_{pH} = pH*k_bTln10, where is the Boltzmann constant and pH=13 for alkaline medium in this study.

Section2. Supporting Figures and Tables

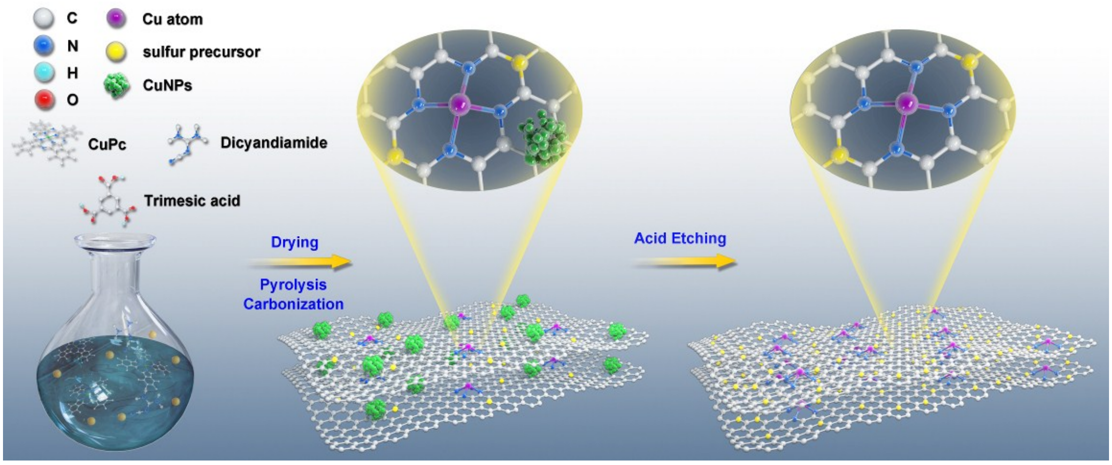

Fig. S1 Schematic illustration for the preparation of Cu-SA/SNC. Typically, copper phthalocyanine (CuPc), dicyandiamide (DCDA), trimesic acid and sulfur precursor were thoroughly mixed in solution and then dried. The Cu-SA/SNC was obtained after pyrolyzing the mixed powder at 900 °C under N_2 atmosphere and acid etching.

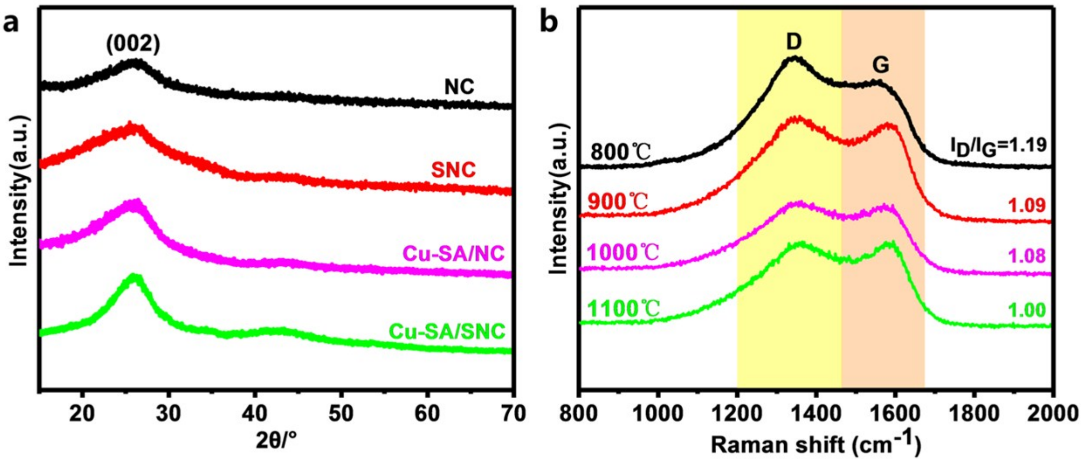

Fig. S2 (a) XRD patterns of Cu-SA/SNC, Cu-SA/NC, SNC and NC. The poor crystallization of the samples means that plenties of defects may exist in the carbon support. (b) Raman spectra of the Cu-SA/SNC samples pyrolyzed at different tempereture. In the Raman spectra, only two characteristic peaks of carbon at 1345 cm^{-1} (D band, disordered/defective carbon) and 1585 cm^{-1} (G band, graphitic carbon) were detected. In the synthetic process, a intermediate temperature (900 °C) was applied, because the just right value of I_D/I_G (1.09). The high ratio of I_D is beneficial for the anchoring of single metal atoms on the carbon matrix. Meanwhile, the high ratio of I_G means the high value of graphitic carbon, playing an important role to improving the conductivity, which is crucial to electrochemical catalysis.[9]

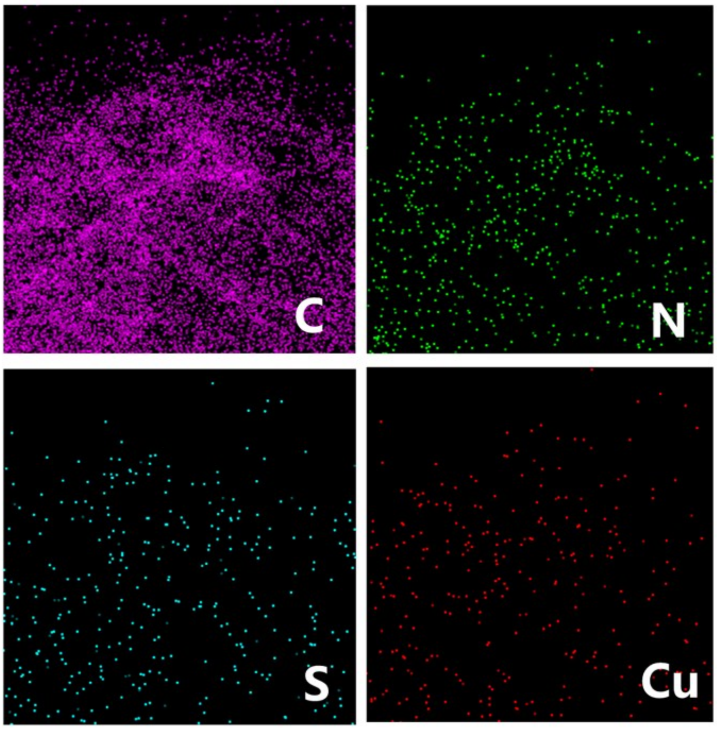

Fig. S3 EDS images of the Cu-SA/SNC. C (purple), N (green), S (blue), and Cu (red) for Cu-SA/SNC. EDS maps indicate the uniform distributions of Cu, S and N on the carbon substrate.

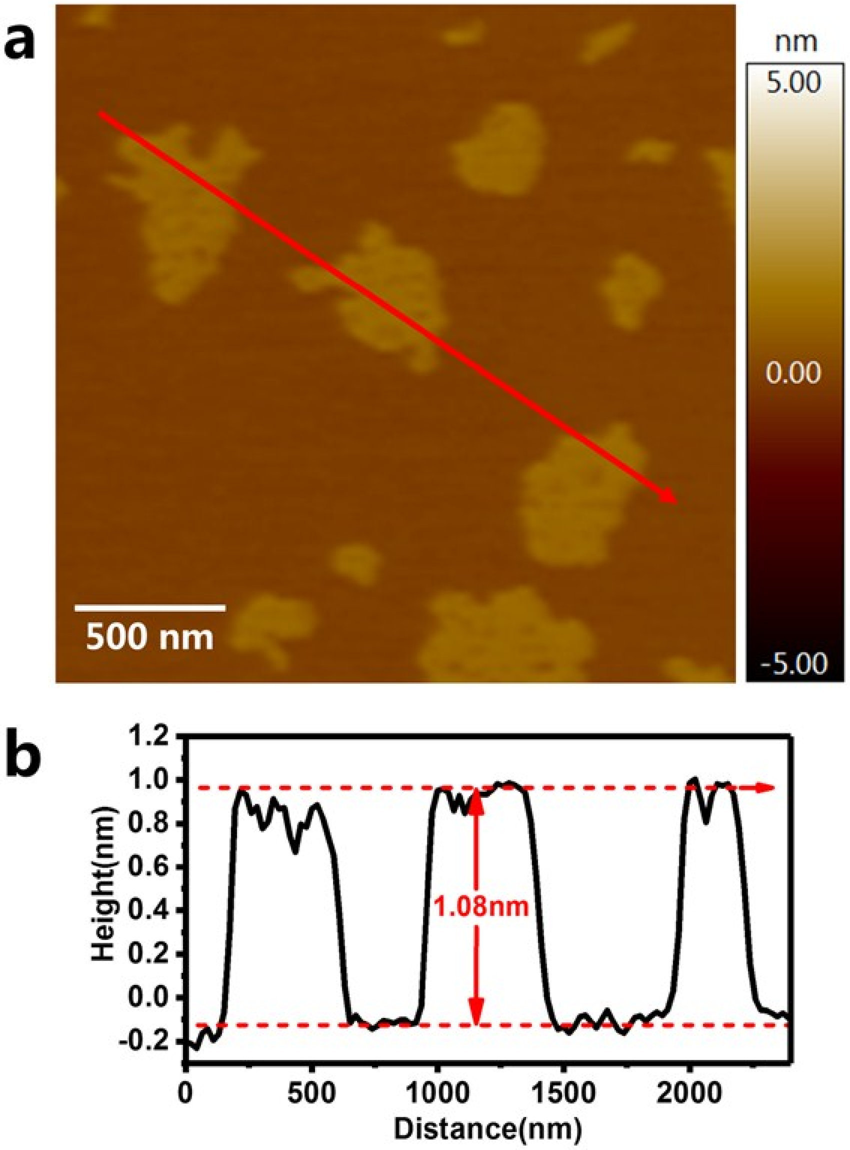

Fig. S4 (a) AFM characterizations of Cu-SA/SNC. (b) The corresponding height profiles of the scans shown in the AFM images. The Cu-SA/SNC is with a thickness about 1 nm.

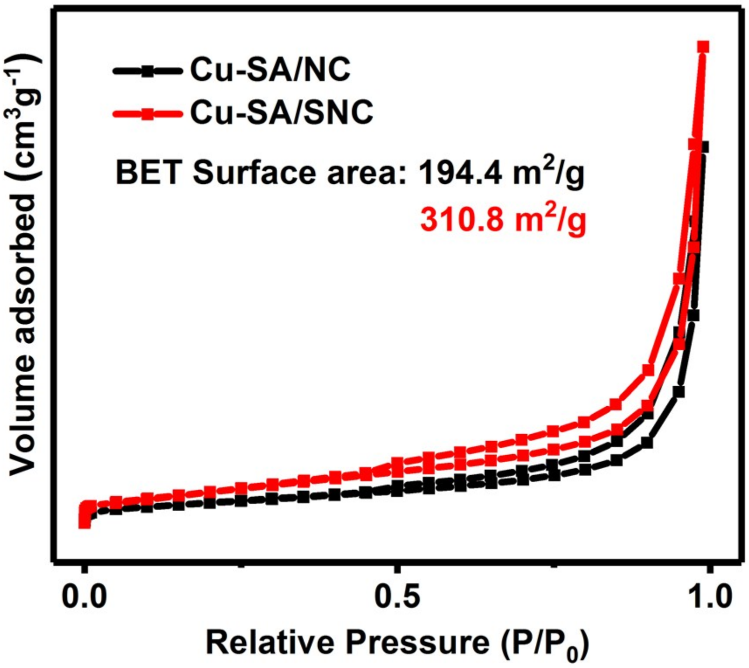

Fig. S5 N_2 adsorption-desorption isotherms of Cu-SA/SNC and Cu-SA/NC. The addition of sulfur plays an important role to improve the specific surface area of the sample, which is also demonstrated by the previous reports.[10]

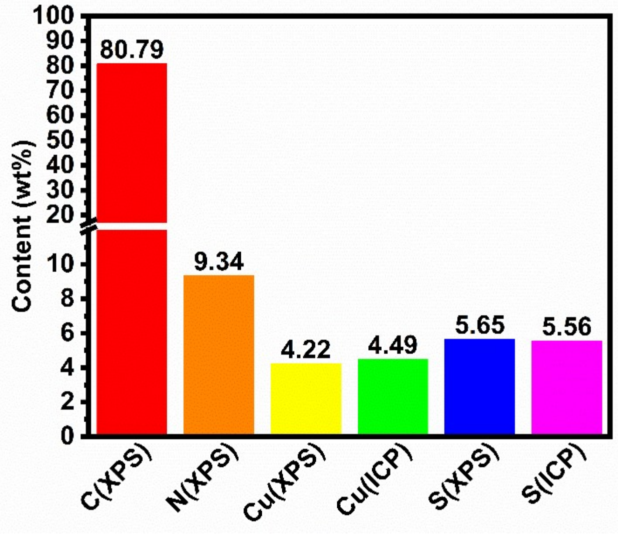

Fig. S6 The weight content percentages of C, N, S and Cu in Cu-SA/SNC measured by XPS analysis, together with the ICP-OES results.

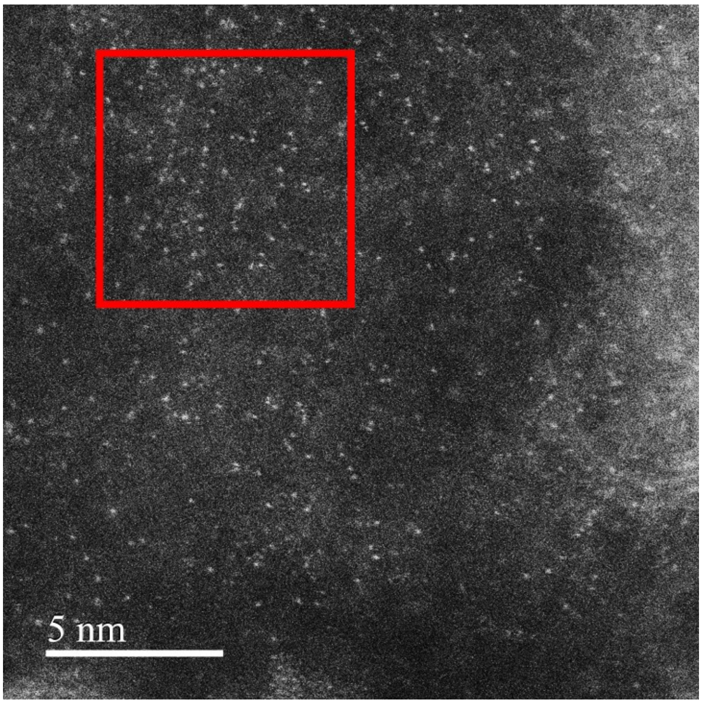

Fig. S7 HAADF-STEM image of Cu-SA/SNC.

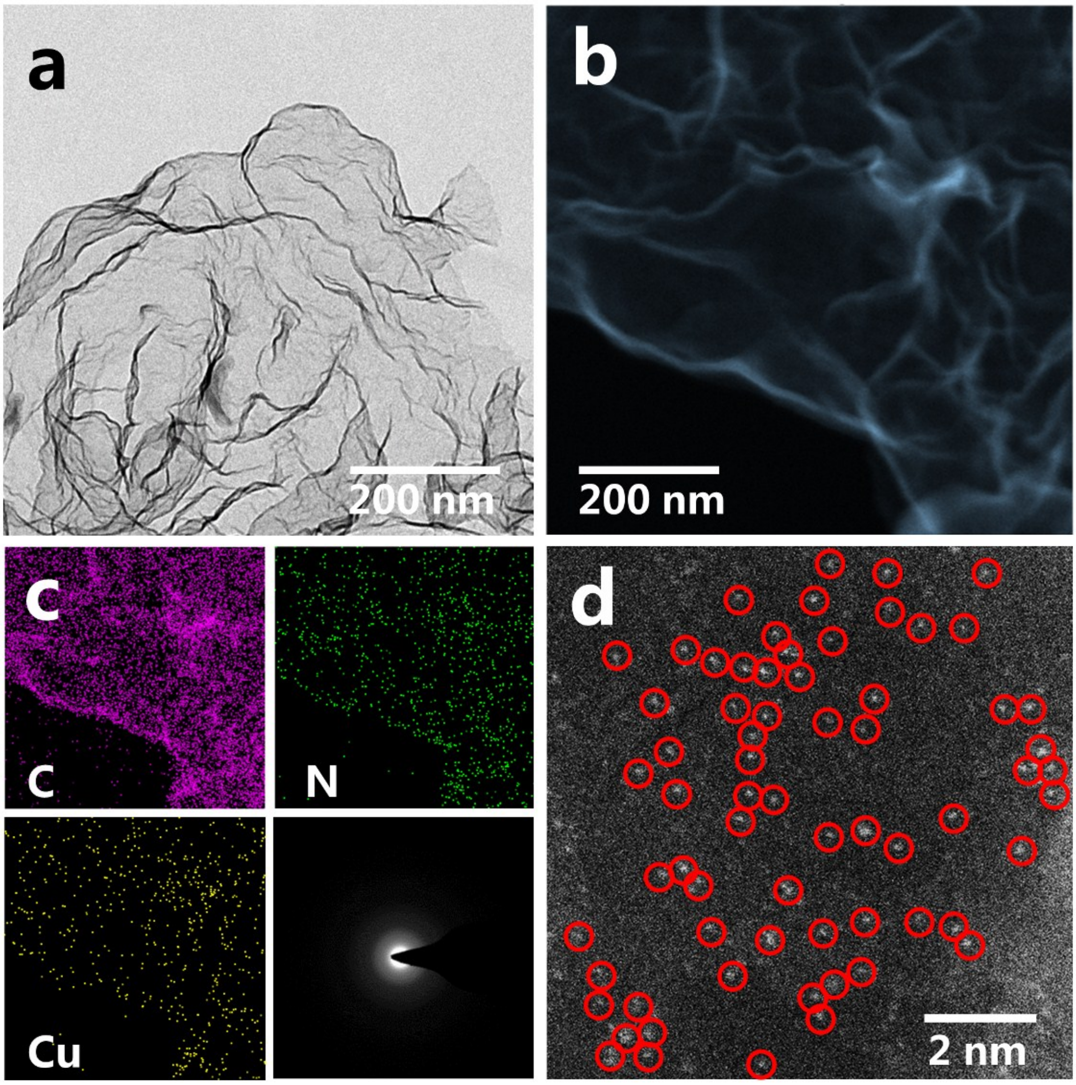

Fig. S8 (a) and (b) TEM images of Cu-SA/NC. (c) EDS images of C (purple), N (green) and Cu (yellow) for Cu-SA/NC, revealing the homogeneous distribution of Cu and N on the carbon support, and the selected area electron diffraction (SAED) pattern. (d) HAADF-STEM image of Cu-SA/NC. The Cu-SA/NC was prepared as the counterpart without sulfur precursor addition. As we can see, the Cu-SA/NC also possesses a graphene-like nanosheet structure, and the Cu and N are uniformly distributed on the carbon substrate. The HADDF-STEM image demonstrates the atomic dispersion of the Cu species. The Cu content in the Cu-SA/NC is 4.6 wt%, according to the ICP-OES analysis.

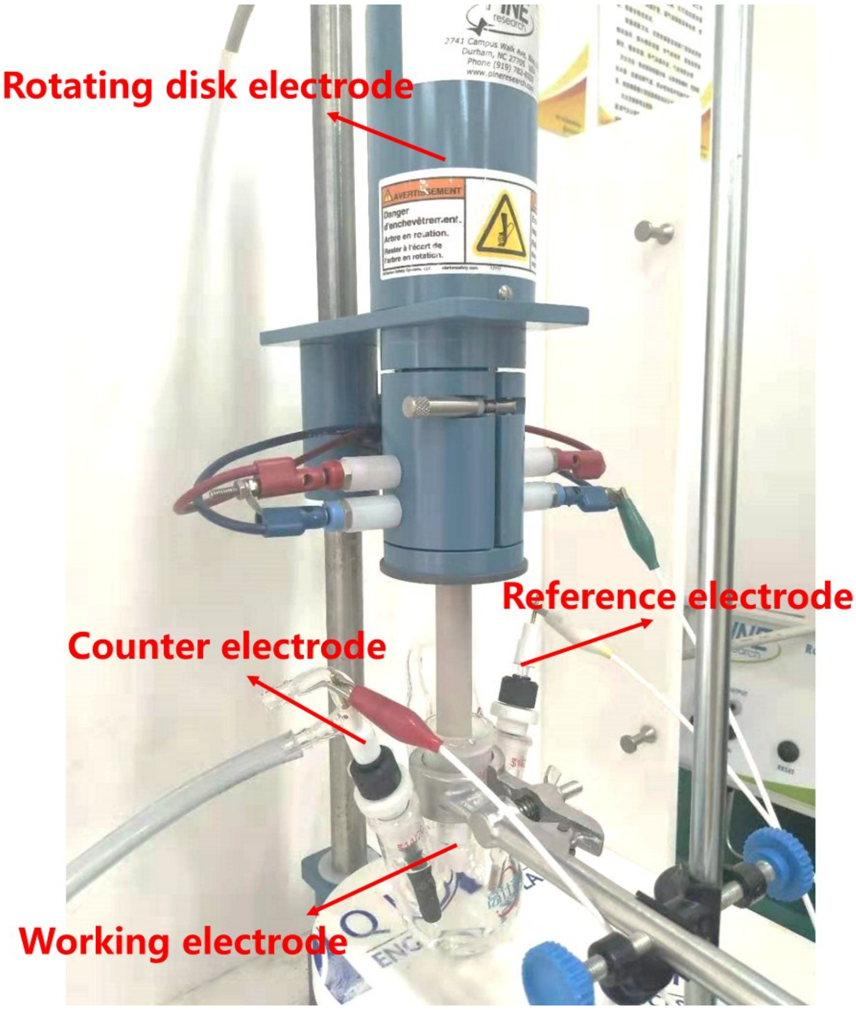

Fig. S9 Photo of the typical three-electrode setup for the electrochemical ORR measurements.

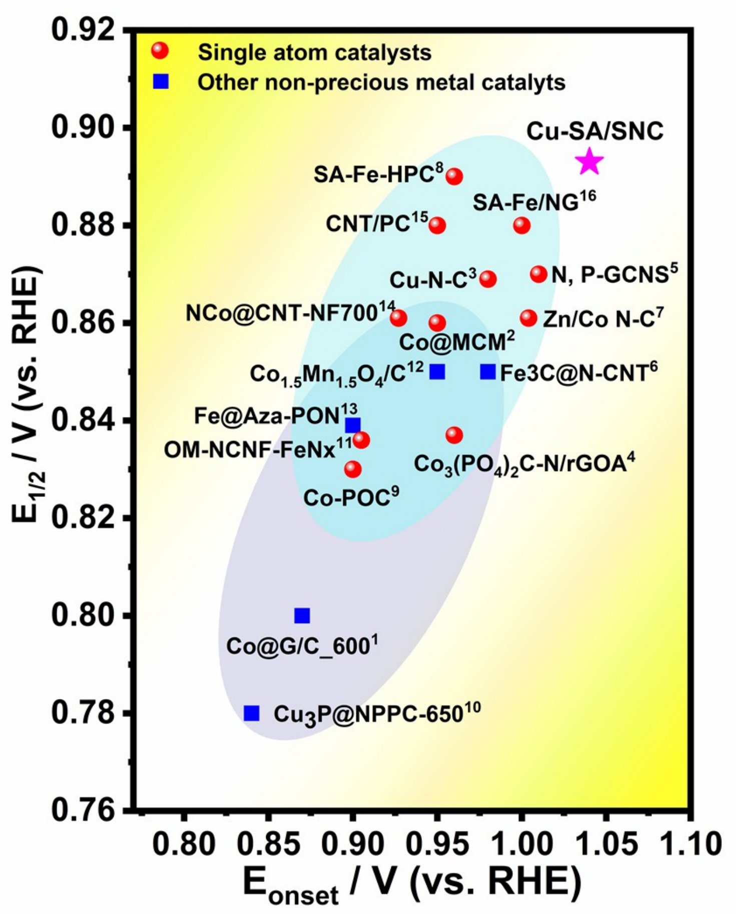

Fig. S10 Comparison of E_{onset} and $E_{1/2}$ values between our catalyst and some recent reported ORR catalysts.

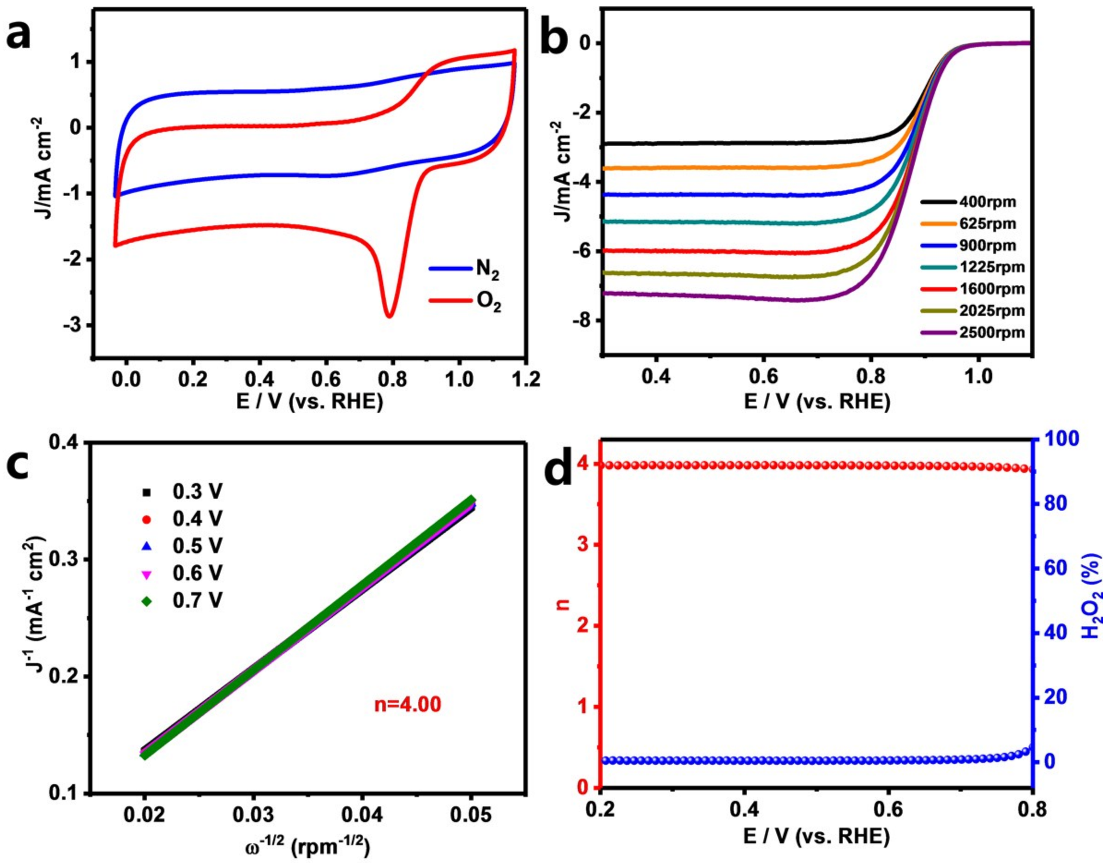

Fig. S11 (a) CV curves of Cu-SA/SNC in O_2- and N_2-saturated 0.1M KOH electrolyte at a scan rate of 50 mV/s. (b) The ORR polarization curves at different rotating rates of Cu-SA/SNC. (c) The corresponding K-L plots and electron transfer number. (e) Electron transfer number (*n*, top) and H_2O_2 yield (bottom) versus potential for Cu-SA/SNC, indicating that the catalytic process at the Cu-SA/SNC electrode underwent a direct four-electron ORR pathway.

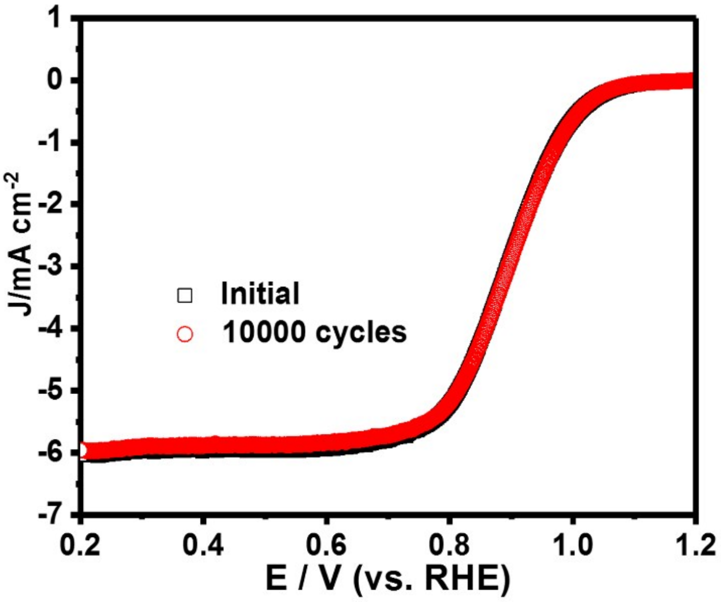

Fig. S12 (a) The long-term durability measurements of Cu-SA/SNC. The durability of Cu-SA/SNC was assessed by cycling the catalyst between 1.2 and 0.2 V *vs* RHE at a sweep rate of 50 mV/s.

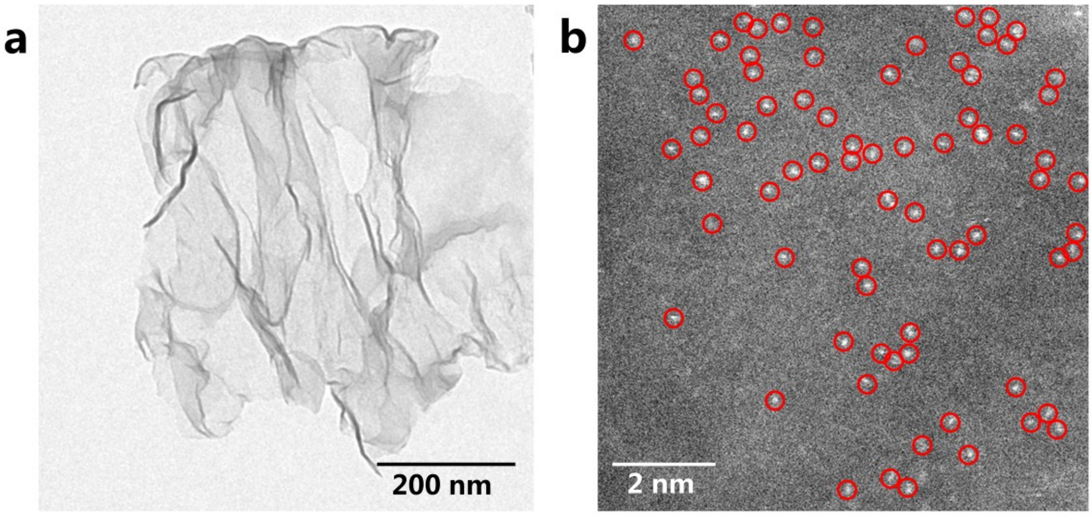

Fig S13 (a) TEM and (b) HAADF-STEM images of Cu-SA/SNC after durability test, reveaIling that the Cu-SA/SNC were still atomically anchored in the carbon matrix.

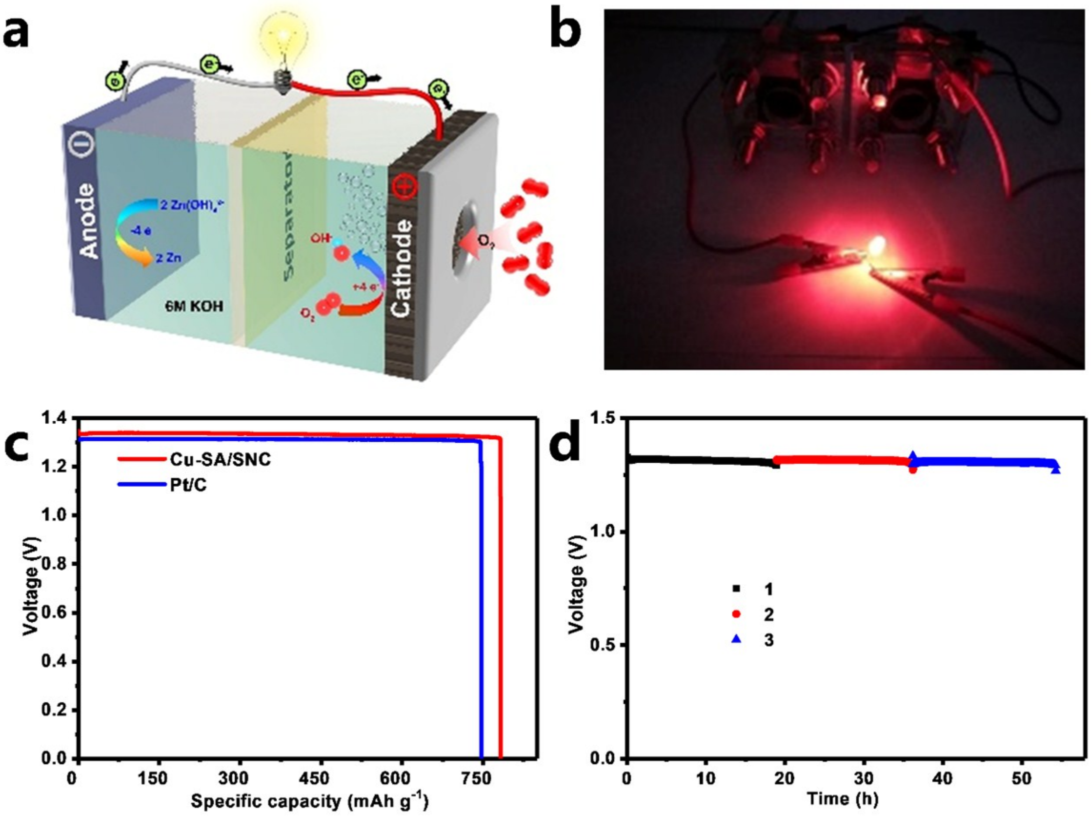

Fig. S14 (a) Schematic illustration of the two-electrode primary Zn-air battery. (b) The photo showing light-emitting diode panel powered by Zn-air batteries based on Cu-SA/SNC. (c) The specific capacity of Cu-SA/SNC and Pt/C-based Zn-air batteries at 5 mA cm^{-2}. (d) Long-term stability of the primary Zn-air battery with Cu-SA/SNC cathode on a current density of 5 mA cm^{-2}. The battery was recharged by re-filling the Zn anode and electrolyte.

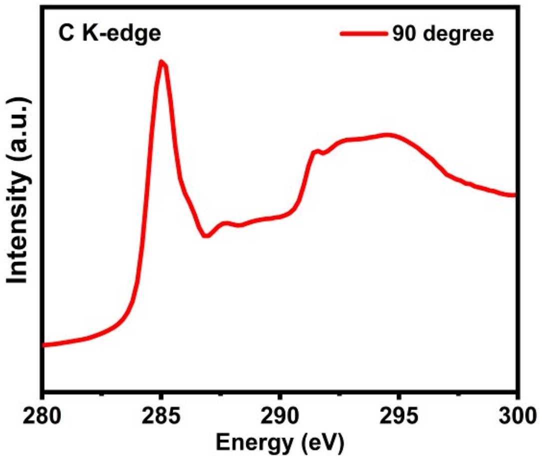

Fig. S15 C K-edge XANES spectra of graphite powder.

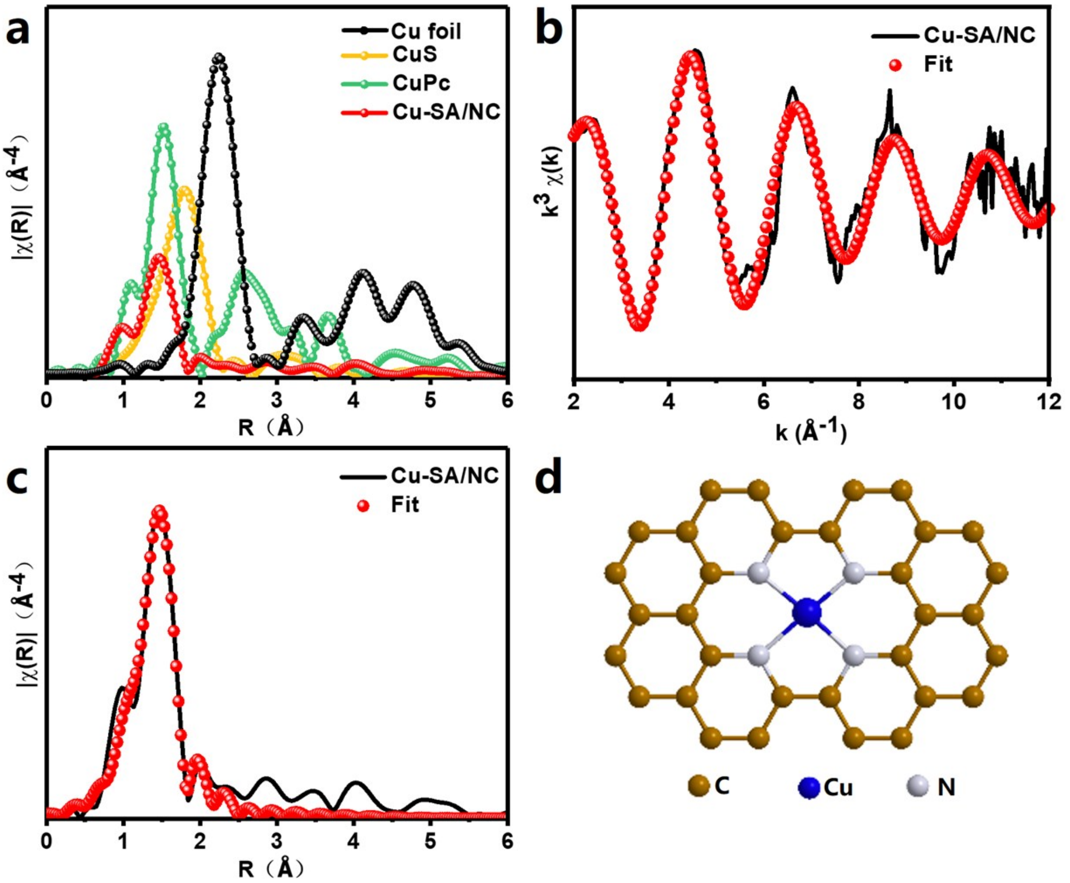

Fig. S16 (a) The ex-situ FT k^3-weighted Cu K-edge EXAFS spectra of Cu-SA/NC and references; (b) and (c) EXAFS fitting curves of Cu-SA/SNC at Cu K-edge (FT range: 2.0-12.0 Å^{-1}, fitting range: 0.5-2.5 Å). (d) Schematic interfacial model of Cu-SA/NC. The best-fit structural parameters are listed in Table S2.

We considered more than three models as we showed in the manuscript. Single, double, triple and quadruple sulfur atoms doped models were considered. The entire screening procedure is described as follows.

Firstly, we considered eleven carbon sites in as the substitution sites for single sulfur (Fig. S17). By comparing the total energy, three relative stable configurations (labeled as C, D, and H, as shown in Fig. S18) were chosen as the models for 1S-doped ORR calculations. Based on this screening step, we determined that sulfur prefers to substitute the carbon site in C-N-Cu six-member heterocycle (site C and D), instead of the carbon site in C-N-Cu five-member heterocycle (site A). Meanwhile, substituting carbon atoms which are far from the Cu-N_4 center (site B, E, F, K, G J and I) is less energetical favorable.

Based on the three relative stable configurations, we also constructed two 2S-doped configurations, where sulfur atoms were not symmetric around Cu atom, as shown in Fig. S19. It should be noted that when two neighboring carbon atoms (CD or DH) were substituted by two sulfur atoms, the planar structure were perturbated since one sulfur atom would bend outward while the other one bends inward. S2-CD is more stable than S2-DH. Both S2-CD and S2-DH were selected to evaluate their ORR performances.

Meanwhile, two 3S-doped Cu-SA/NC configurations were also constructed as shown in Fig. S20. Similar to S2-CD or S2-DH, there is a significant distortion near S-S-S zone. S3-CDH is more stable than S3-CDC'. Only S3-CDH was chosen to carry out the ORR calculation.

As for 4S-doped Cu-SA/NC configurations, the substituted carbon atoms were chosen from C, D, H and their symmetrical sites only. The configurations were built as shown in Fig. S21. Among them, the most stable one, S4-CDC'D'was adopted for ORR calculation.

The free energy diagrams together with the configurations for adsorbates on *n*S-doped models (n = 1, 2, 3, and 4) were shown in Fig. S22-S28. All the ORR performances for configurations from Fig. S22-S28 could not be comparable with it for S-d Cu-N_4-C_8S_2 (each step is down-hill) in the manuscript.

Based on the results of configurations optimization and the ORR calculation, it is determined that sulfur prefers to substitute the carbon site in C-N-Cu six-member heterocycle, instead of the carbon site in C-N-Cu five-member heterocycle. Meanwhile, replacing two neighboring carbon atoms would cause significant distortion, which shows negative impact for improving ORR performance. In addition, the ORR performance when only one carbon was replaced (at least for the ones we considered) could not match the ORR performance of the S-d Cu-N_4-C_8S_2 configuration.

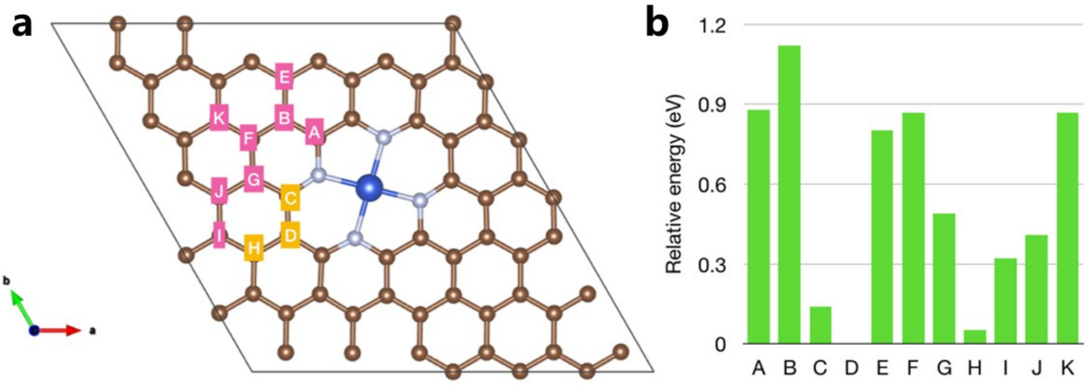

Fig. S17 (a) Labels for sulfur substituted sites. (b) The relative energies (units: eV) for the sulfur substituted Cu-SA/NC models.

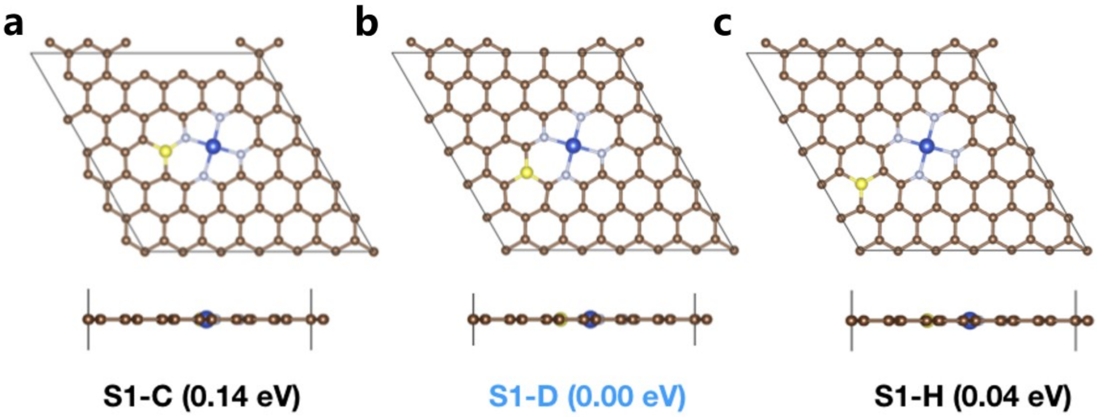

S1-C (0.14 eV)

S1-D (0.00 eV)

S1-H (0.04 eV)

Fig. S18 Top and side views for S1-C (a), S1-D (b) and S1-H (c), as well as the relative energies (in parentheses).

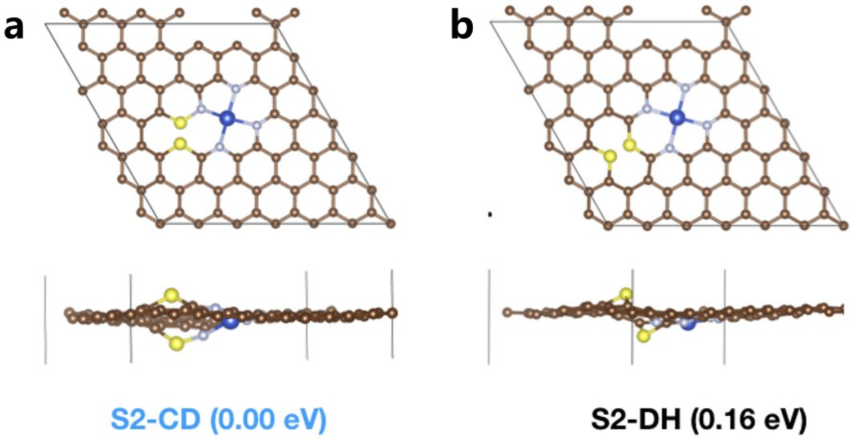

S2-CD (0.00 eV)

S2-DH (0.16 eV)

Fig. S19 Top and side views for S2-CD (a) and S2-DH (b), as well as the relative energies (in parentheses).

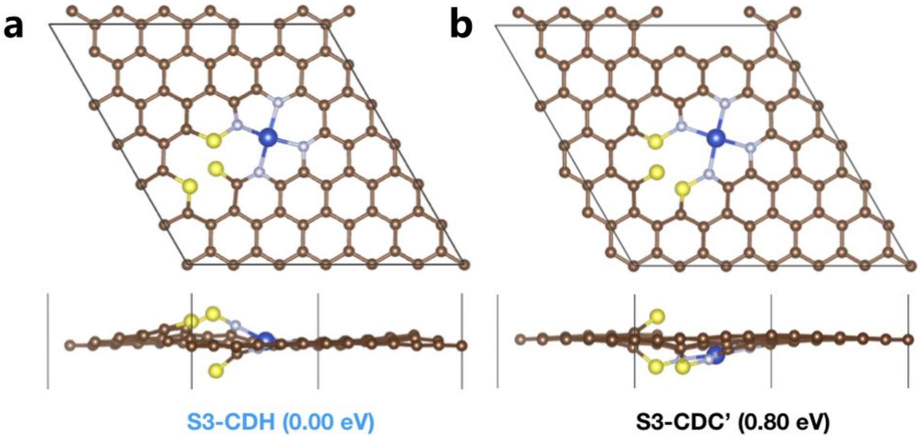

S3-CDH (0.00 eV)

S3-CDC’ (0.80 eV)

Fig. S20 Top and side views for S3-CDH (a) and S3-CDC’ (b), as well as the relative energies (in parentheses).

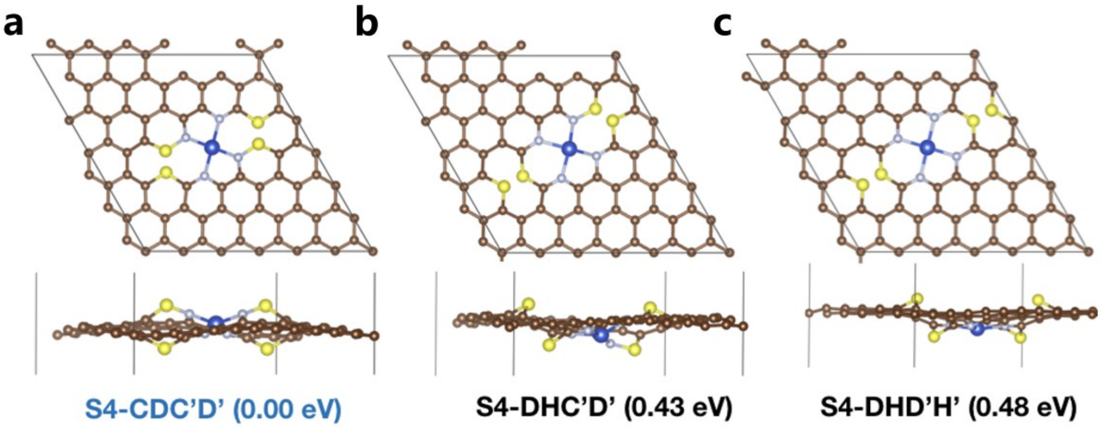

S4-CDC’D’ (0.00 eV)

S4-DHC’D’ (0.43 eV)

S4-DHD’H’ (0.48 eV)

Fig. S21 Top and side views for S4-CDC’D’ (a), S4-DHC’D’ and S4-DHD’H’ (b), as well as the relative energies (in parentheses).

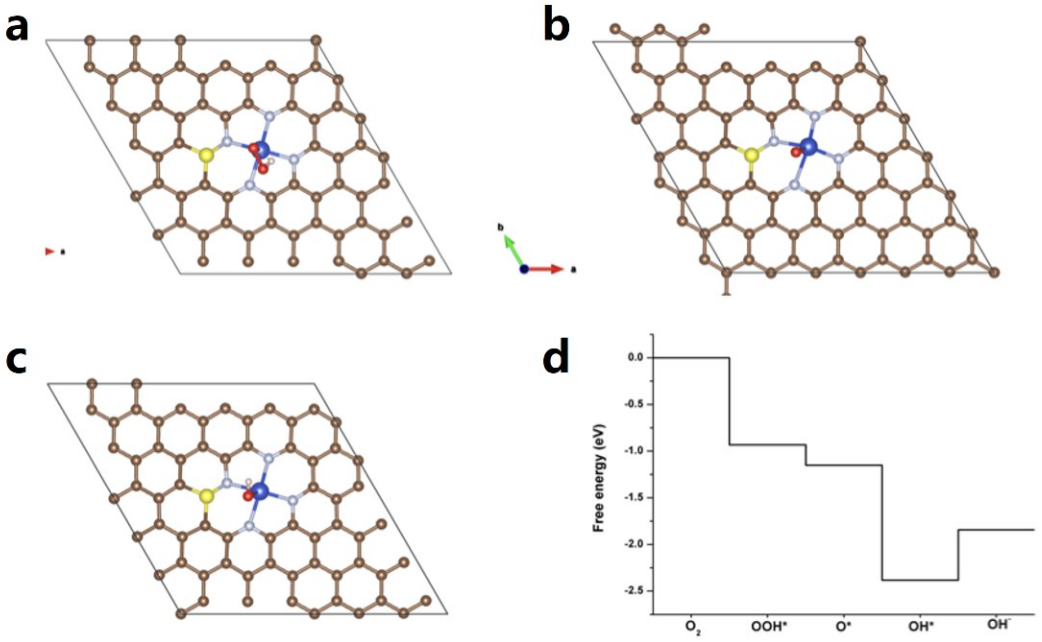

Fig. S22 The free energy diagram together with the configurations for adsorbates (OOH, O and OH) on S1-C.

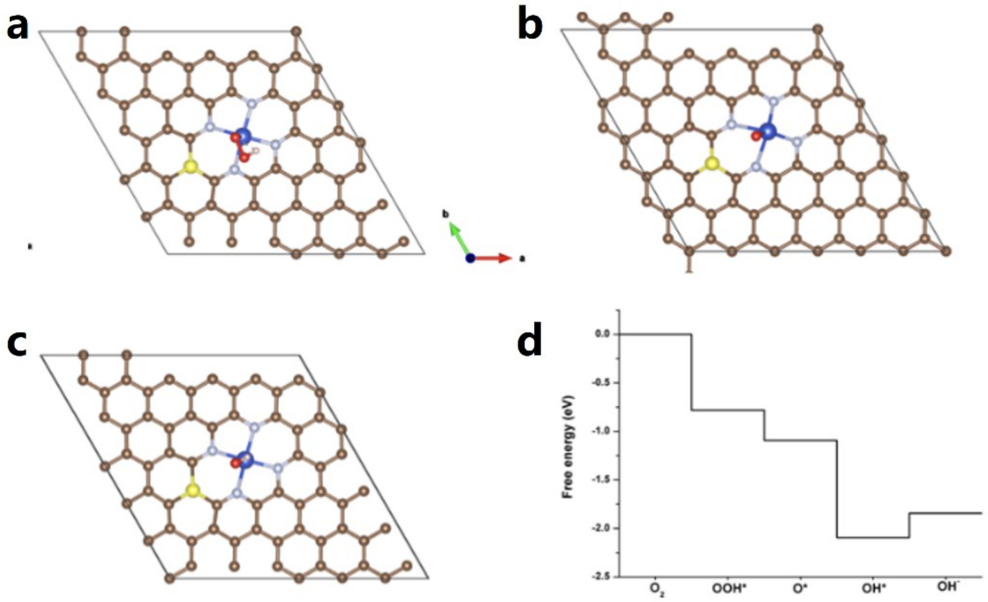

Fig. S23 The free energy diagram together with the configurations for adsorbates (OOH, O and OH) on S1-D.

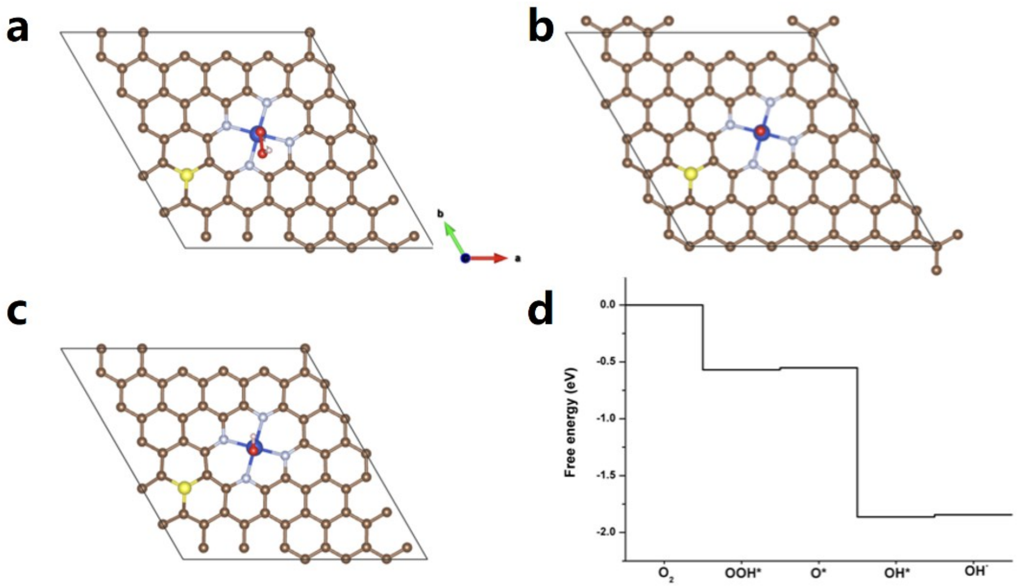

Fig. S24 The free energy diagram together with the configurations for adsorbates (OOH, O and OH) on S1-H.

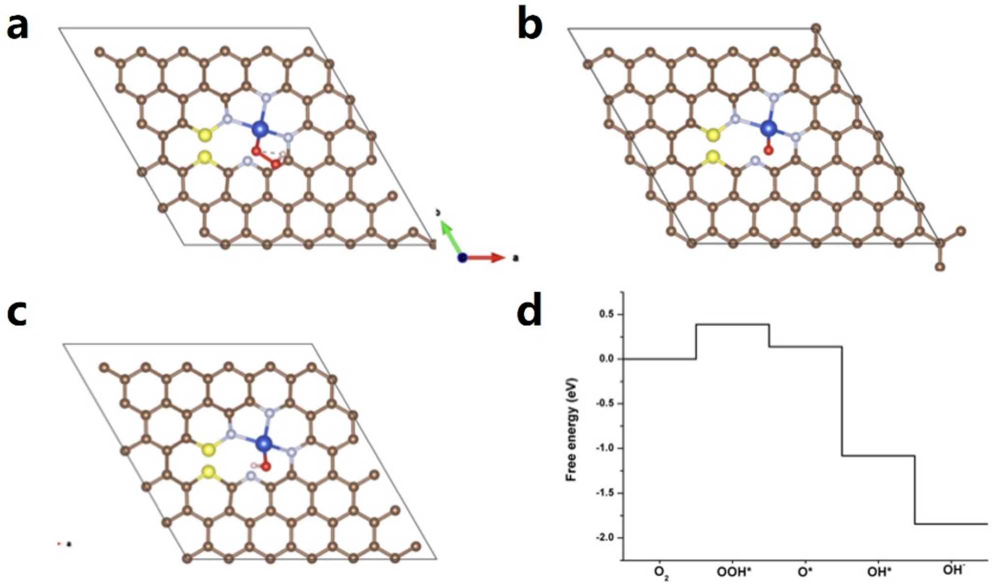

Fig. S25 The free energy diagram together with the configurations for adsorbates (OOH, O and OH) on S2-CD.

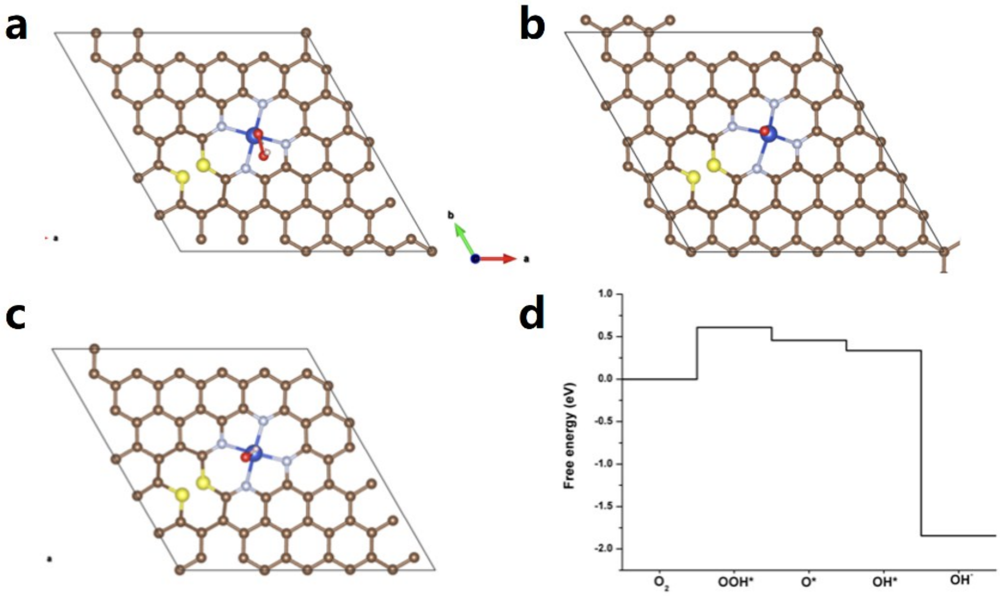

Fig. S26 The free energy diagram together with the configurations for adsorbates (OOH, O and OH) on S2-DH.

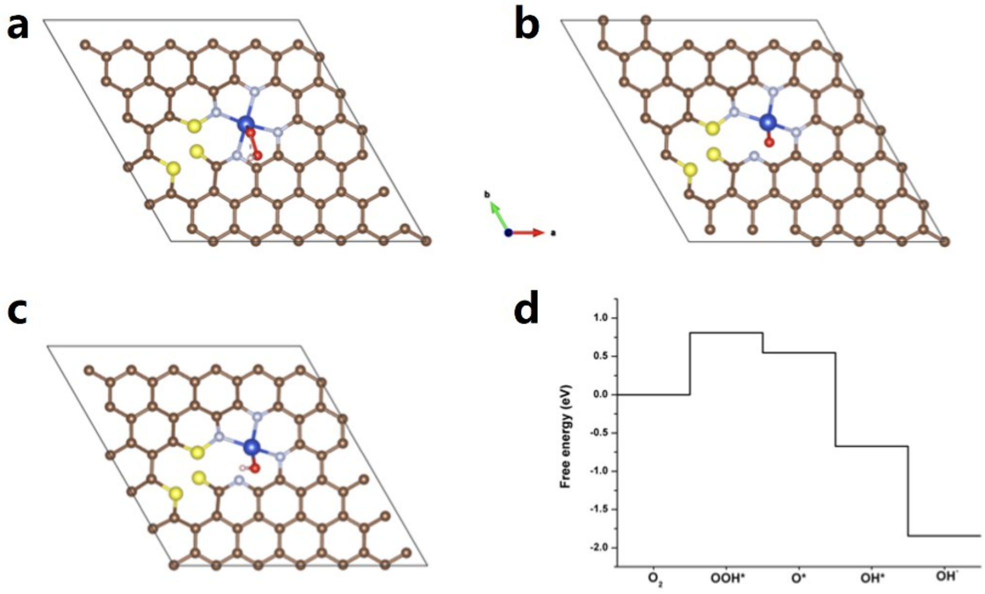

Fig. S27 The free energy diagram together with the configurations for adsorbates (OOH, O and OH) on S3-CDH.

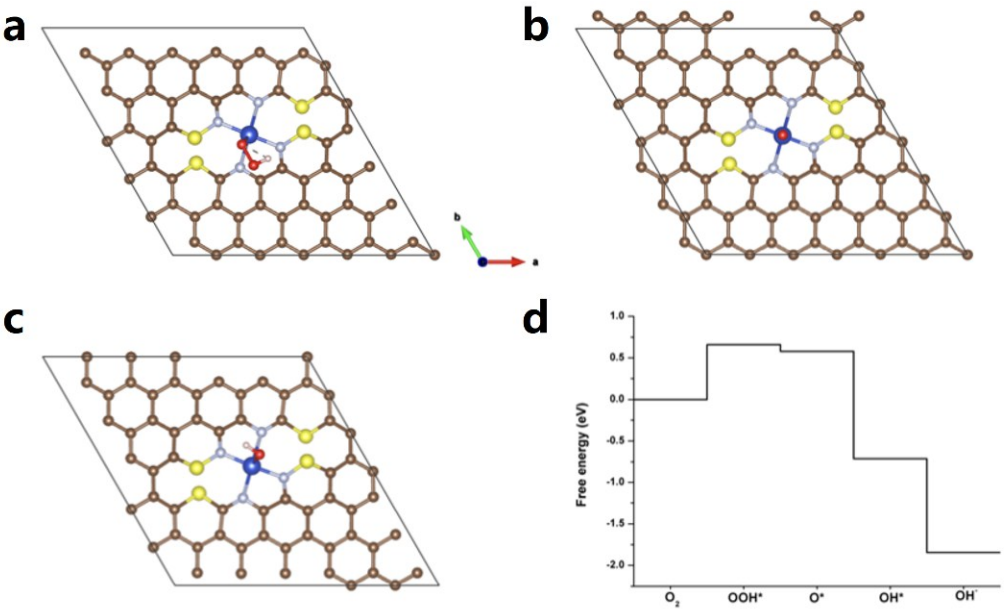

Fig. S28 The free energy diagram together with the configurations for adsorbates (OOH, O and OH) on S4-CDC'D'.

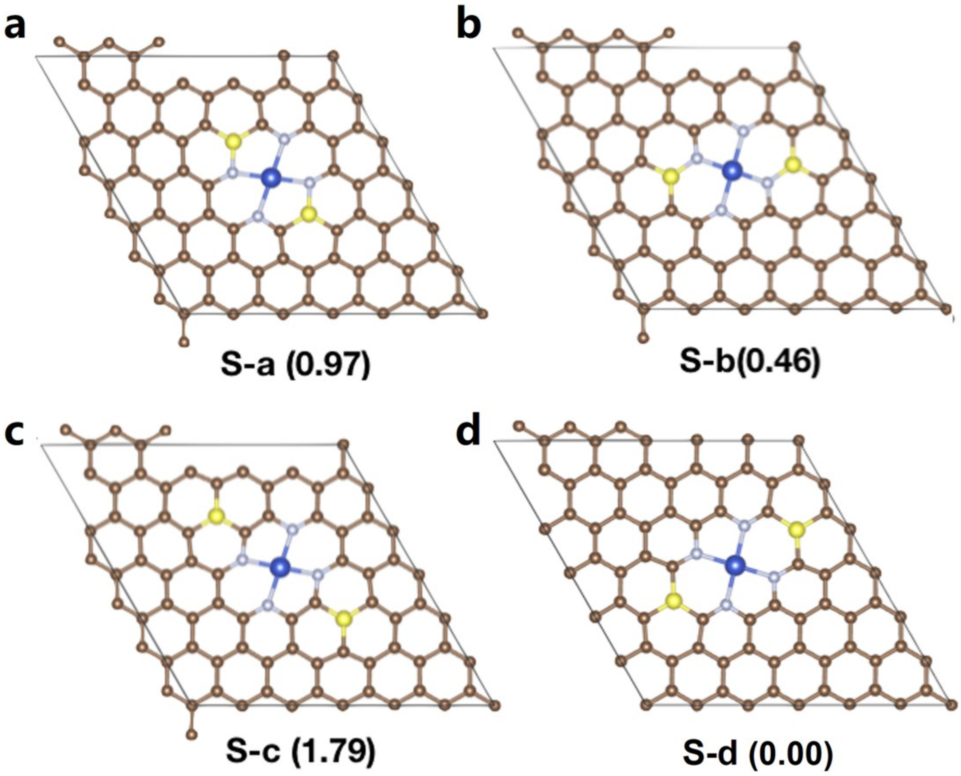

Fig. S29 Optimized interfacial models and the corresponding relative energy (unit: eV). Color code: C atoms, brown; N atoms, purple; S atoms, yellow; Cu atoms, blue.

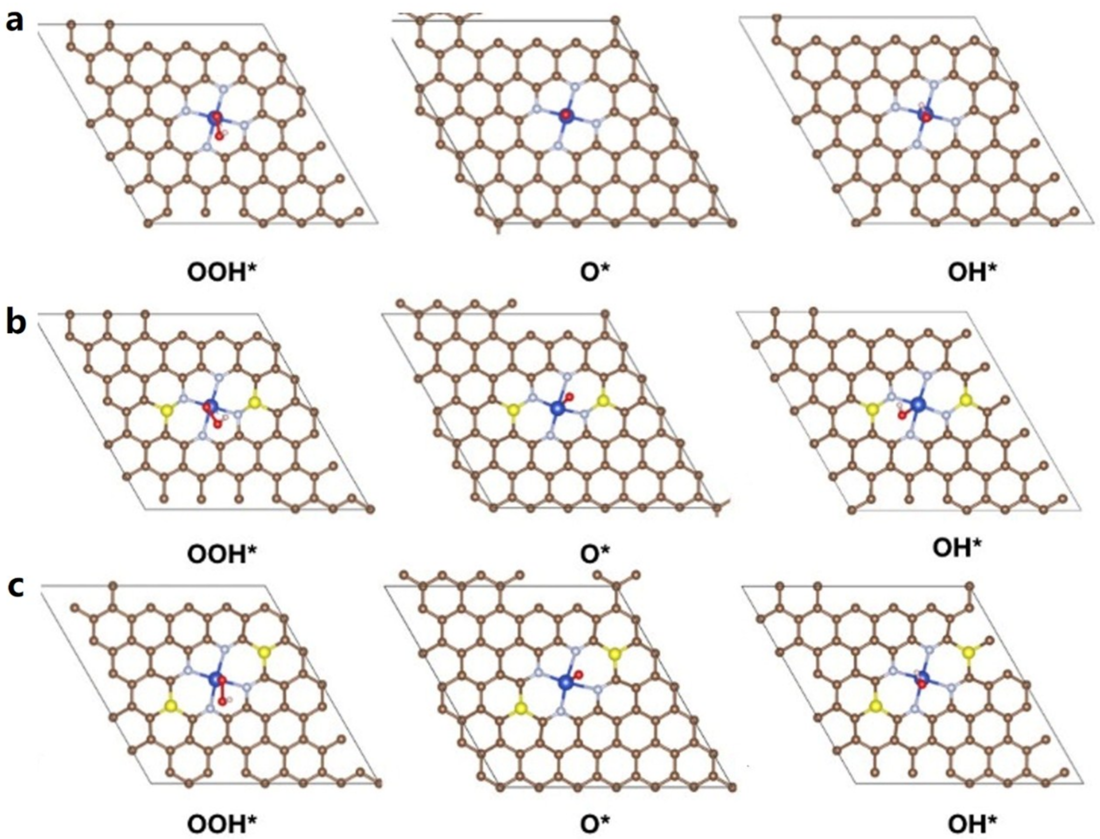

Fig. S30 The adsorption configurations for intermediates (OOH*, O* and OH*) on Cu-SA/NC (a: Cu-N_4-C_{10}) and two S-modified Cu-SA/SNC interfacial models (b: S-b Cu-N_4-C_8S_2, c: S-d Cu-N_4-C_8S_2). Color code: C atoms, brown; N atoms, purple; S atoms, yellow; Cu atoms, blue; H atoms, white; O atoms, red.

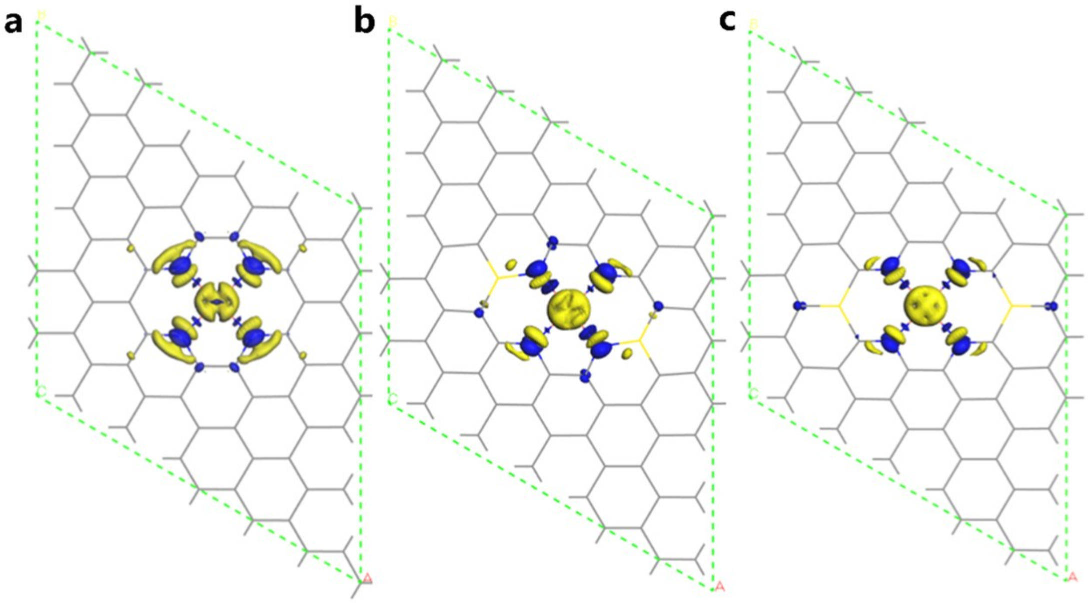

Fig. S31 The calculated charge density differences for Cu-SA/NC (a: Cu-N_4-C_{10}) and two S-modified Cu-SA/SNC interfacial models (b: S-b Cu-N_4-C_8S_2, c: S-d Cu-N_4-C_8S_2). Blue and yellow areas represent charge density enriched and depleted, respectively. The isosurface is at a value of 0.05 electrons/Å^3.

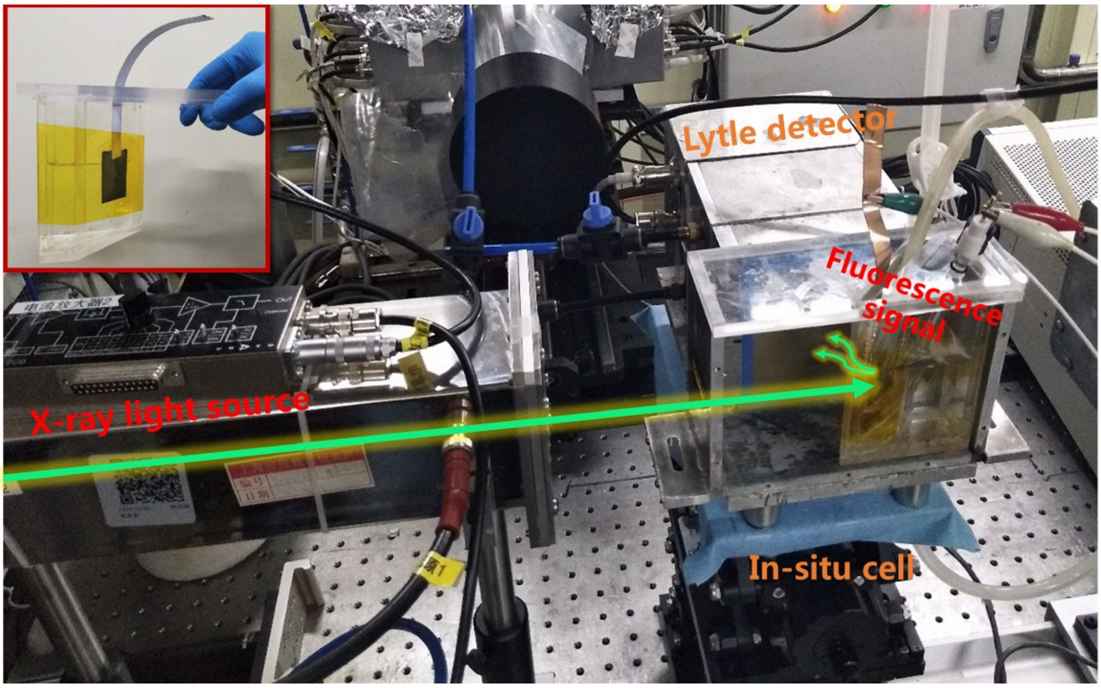

Fig. S32 The detail of the in-situ X-ray absorption spectroscopy measurement. The device is set up at 14W1 beam line with the support from SSRF, where the X-ray induced fluorescence model is applied. CE, counter electrode; WE, working electrode; RE, reference electrode.

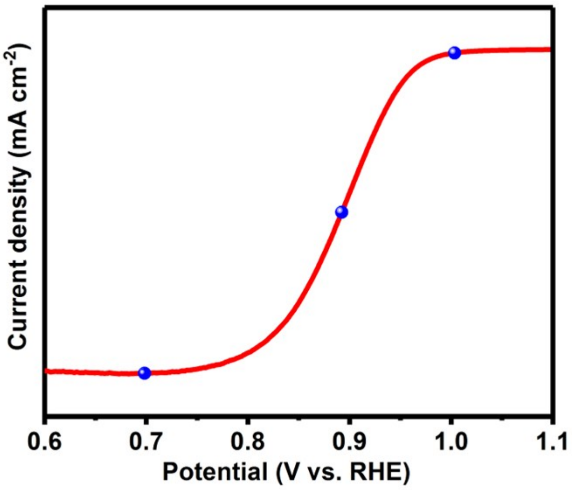

Fig. S33 ORR polarization curve for Cu-SA/SNC under in-situ XAFS condition (1.0 V, 0.893 V and 0.7 V *vs* RHE).

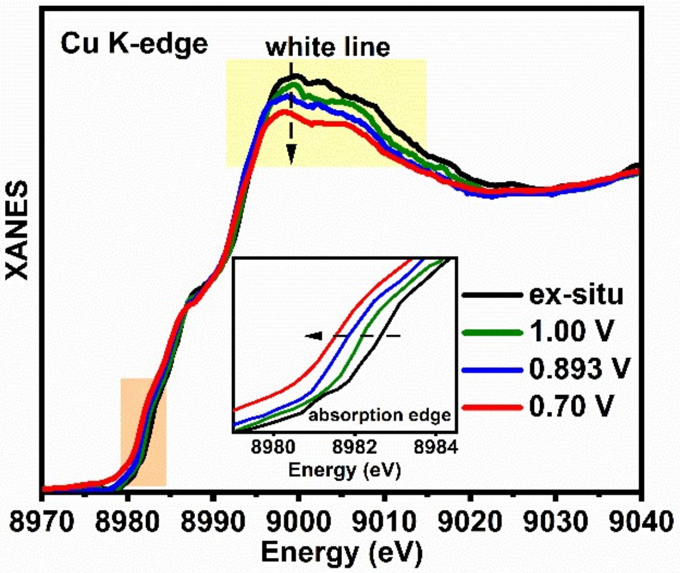

Fig. S34 Cu K-edge XANES spectra of Cu-SA/SNC at various potentials during ORR.

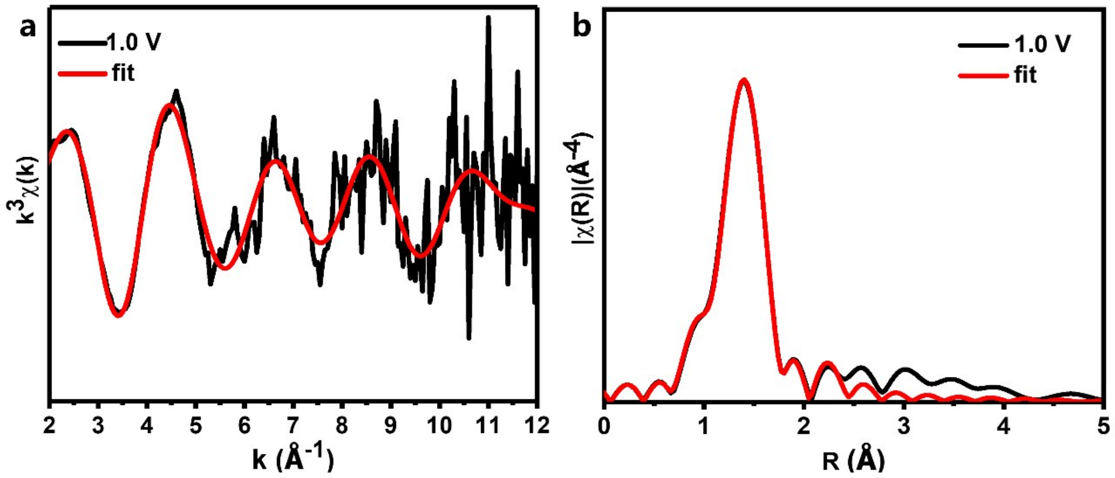

Fig. S35 (a) *k* space EXAFS fitting spectra and (b) FT-EXAFS fitting spectra of Cu-SA/SNC (FT range: 2.0-12.0 $Å^{-1}$, fitting range: 0.5-2.0 Å) under 1.0 V *vs* RHE. The best-fit structural parameters are listed in Table S3.

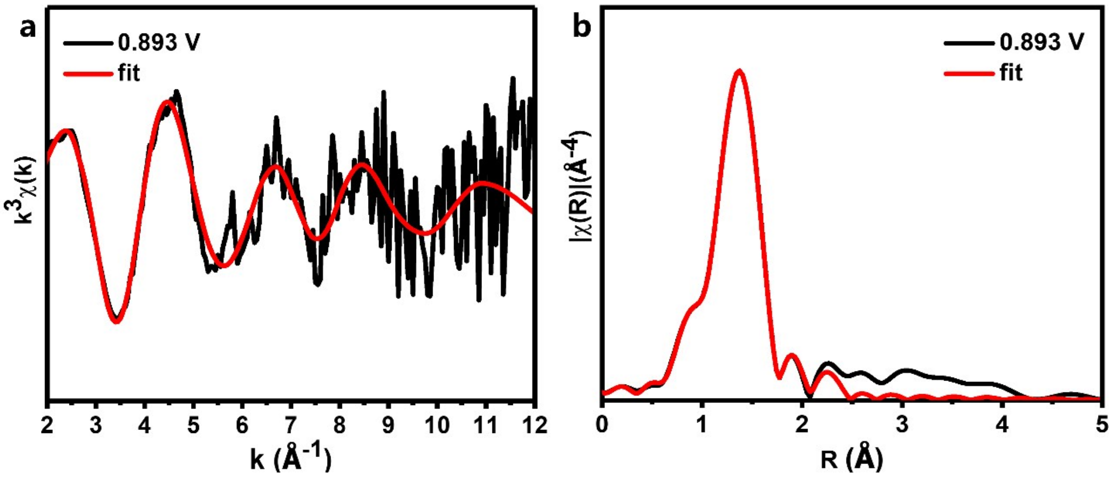

Fig. S36 (a) *k* space EXAFS fitting spectra and (b) FT-EXAFS fitting spectra of Cu-SA/SNC (FT range: 2.0-12.0 Å^{-1}, fitting range: 0.5-2.0 Å) under 0.893 V *vs* RHE. The best-fit structural parameters are listed in Table S3.

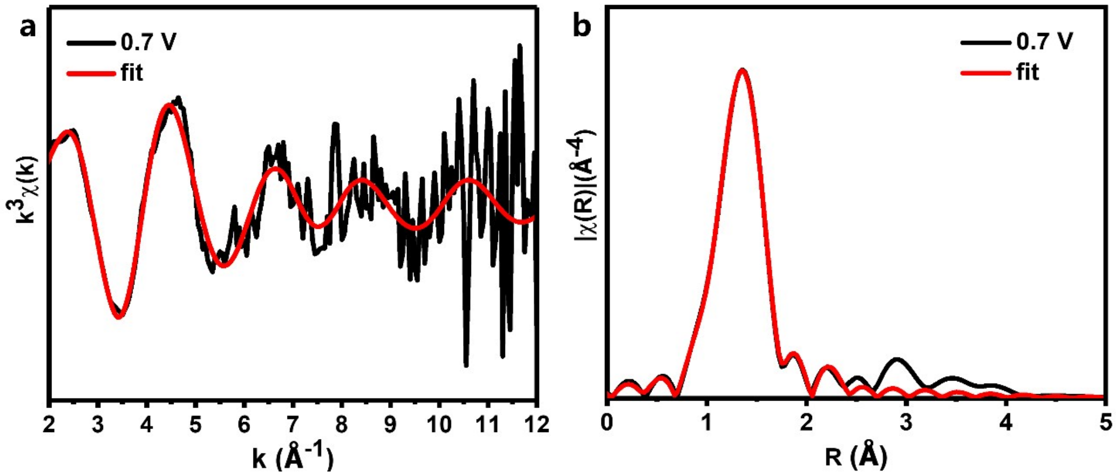

Fig. S37 (a) *k* space EXAFS fitting spectra and (b) FT-EXAFS fitting spectra of Cu-SA/SNC (FT range: 2.0-12.0 Å^{-1}, fitting range: 0.5-2.0 Å) under 0.7 V *vs* RHE. The best-fit structural parameters are listed in Table S3.

Table S1. Comparison of ORR performance between Cu-SA/SNC and other non-precious catalysts reported in the literatures under O_2-saturated 0.1 M KOH.

No.	*Catalyst*	*Onset potential (V vs. RHE)*	*Half-wave potential (V vs. RHE)*	*loading (mg cm^{-2})*	*Reference*
	Cu-SA/SNC	**1.04**	**0.893**	**0.102**	**This work**
1	Co@G/C_600	0.87	0.8	0.152	Energy Environ. Sci., 2019,12, 2200-2211
2	Co@MCM	0.95	0.86	-	Energy Environ. Sci., 2018,11, 1980-1984
3	Cu-N-C	0.98	0.869	3.31	Energy & Environ. Sci. 2018, 11, 2263.
4	Co3(PO4)2C-N/rGOA	0.96	0.837	0.25	Energy Environ. Sci., 2016,9, 2563-2570
5	N,P-GCNS	1.01	0.87	-	Energy Environ. Sci., 2016,9, 357-390
6	Fe3C@N-CNT	0.98	0.85	-	Energy Environ. Sci., 2016,9, 3092-3096
7	Zn/Co N-C	1.004	0.861	0.255	Angew. Chem. Int. Ed. 2019, 131, 2648-2652.
8	SA-Fe-HPC	0.96	0.89	-	Angew. Chem. Int. Ed. 2018, 57, 9038-9043.
9	Co-POC	0.9	0.83	0.100	Adv. Mater. 2019, 1900592.
10	Cu_3P@NPPC-650	0.84	0.78	0.2	Adv. Mater. 2018, 30, 1703711.
11	OM-NCNF-FeNx	0.905	0.836	0.250	Adv. Mater. 2018, 30, 1802669.
12	$Co_{1.5}Mn_{1.5}O_4$/C	0.95	0.85	0.1	J. Am. Chem. Soc. 2019, 141, 1463−1466
13	Fe@Aza-PON	0.9	0.839	0.159	J. Am. Chem. Soc. 2018, 140, 1737-1742.
14	NCo@CNT-NF700	0.927	0.861	0.2	J. Am. Chem. Soc. 2018, 140, 15393-15401.
15	CNT/PC	0.95	0.88	0.8	J. Am. Chem. Soc. 2016, 138, 15046-15056.
16	SA-Fe/NG	1.00	0.88	0.6	PNAS 2018, 115, 6626-6631.

Table S2. Structural parameters extracted from the Cu K-edge EXAFS fitting. (S_0^2=0.86)

sample	*Scattering pair*	*CN*	*R(Å)*	*$\sigma^2(10^{-3}Å^2)$*	**ΔE_0(eV)**	***R factor***
Cu-SA/SNC	Cu-N	4.0±0.6	1.95±0.01	6.4±0.5	2.5±0.5	0.004
Cu-SA/NC	Cu-N	3.9±0.5	2.00±0.01	5.8±0.4	2.0±0.5	0.005
Cu foil	Cu-Cu	12*	2.55±0.01	7.9±0.8	3.0±0.4	0.003

S_0^2 is the amplitude reduction factor; CN is the coordination number; R is interatomic distance (the bond length between central atoms and surrounding coordination atoms); σ^2 is Debye-Waller factor (a measure of thermal and static disorder in absorber-scatterer distances); ΔE_0 is edge-energy shift (the difference between the zero kinetic energy value of the sample and that of the theoretical model). R factor is used to value the goodness of the fitting.

* This value was fixed during EXAFS fitting, based on the known structure.

Error bounds that characterize the structural parameters obtained by EXAFS spectroscopy were estimated as N ± 20%; R ± 1%; σ^2 ± 20%; ΔE_0 ± 20%.

Table S3. Mulliken charge population for Cu, surrounding N atoms and the doping S atoms in the considered models. S_L and S_R indicate the S atom on the left and right of Cu, respectively.

	Cu	N_1	N_2	N_3	N_4	S_L	S_R
S-free	1.46	-0.48	-0.48	-0.48	-0.48	-	-
S-b	1.24	-0.77	-0.49	-0.77	-0.49	0.96	0.96
S-d	1.14	-0.46	-0.46	-0.46	-0.47	0.74	0.74

Table S4. Structural parameters extracted from the Cu K-edge EXAFS fitting. (S_0^2=0.86)

sample	***Scattering pair***	***CN***	***R(Å)***	***σ^2(10^{-3}Å^2)***	**ΔE_0(eV)**	***R factor***
Cu-SA/SNC at 1.0V	Cu-N	4.1±0.5	1.91±0.01	5.7±0.4	2.0±0.5	0.004
	Cu-O	1.0±0.6	1.93±0.01	6.1±0.4		
Cu-SA/SNC at 0.893V	Cu-N	3.8±0.6	1.90±0.01	4.9±0.5	2.0±0.5	0.007
	Cu-O	1.1±0.4	1.91±0.01	5.4±0.7		
Cu-SA/SNC at 0.7V	Cu-N	3.9±0.3	1.91±0.01	6.3±0.8	2.0±0.5	0.006
	Cu-O	1.0±0.3	1.90±0.01	5.8±0.5		

S_0^2 is the amplitude reduction factor; CN is the coordination number; R is interatomic distance (the bond length between central atoms and surrounding coordination atoms); σ^2 is Debye-Waller factor (a measure of thermal and static disorder in absorber-scatterer distances); ΔE_0 is edge-energy shift (the difference between the zero kinetic energy value of the sample and that of the theoretical model). R factor is used to value the goodness of the fitting.

Error bounds that characterize the structural parameters obtained by EXAFS spectroscopy were estimated as N ± 20%; R ± 1%; σ^2 ± 20%; ΔE_0 ± 20%.

References

1. B. Ravel and M. Newville, *Phys. Scr.,* 2005, **2005**, 1007.
2. A. Grossmann, M. Holschneider, R. Kronland-Martinet and J. Morlet. *Adv. Electron. Electron Phys.,* 1986.
3. H. Funke and A. C. Scheinost. *Phys. Rev. B,* 2005, **71**, 094110.
4. Wavemetrics, IGOR, 6.0.3.1, (1988–2008), Lake Oswego.
5. A. Grossmann and J. Morlet. *SIAM J. Math. Anal.*, 1984, **15**, 723–736.
6. H. Funke, M. Chukalinac and A. C. Scheinost. *J. Synchrotron Rad.*, 2007, **14**, 426–432.
7. S. J. Clark, M. D. Segall, C. J. Pickard, P. J. Hasnip, M. I. Probert, K. Refson and M. C. Payne, *Z. Kristallogr.,* 2005, **220,** 567.
8. J. P. Perdew, K. Burke and M. Ernzerhof, *Phys. Rev. Lett.,* 1996, **77,** 3865.
9. R. Jiang, L. Li, T. Sheng, G. Hu, Y. Chen and L. Wang, *J. Am. Chem. Soc.* 2018, **140,** 11594.
10. Y. Qiao, P. Yuan, Y. Hu, J. Zhang, S. Mu, J. Zhou, H. Li, H. Xia, J. He and Q. Xu, *Adv. Mater.,* 2018, **30,** 1804504.